Materials & Design 265 (2026) 116020

Contents lists available at ScienceDirect

Materials & Design

journal homepage: www.elsevier.com/locate/matdes

Oxidation-controlled creep response of miniaturized Waspaloy specimens in a hydrogen-containing atmosphere

O. Nagel [a,*], C. Tang [b], L. Haußmann [a], A. Demirci [a], S. Vollath [a], M. Fritton [c], R. Gilles [c], M. Göken [a], B. Gorr [b], S. Neumeier [a]

[a] Friedrich-Alexander-Universität Erlangen-Nürnberg, Department of Materials Science & Engineering, Institute I: General Materials Properties, Erlangen, Germany
[b] Karlsruhe Institute of Technology, Institute for Applied Materials – Applied Materials Physics, Karlsruhe, Germany
[c] Technische Universität München, Heinz Maier-Leibnitz Zentrum, Garching, Germany

ARTICLE INFO

Keywords:
Ni-based superalloy
Hydrogen embrittlement
Creep
Hydrogen-containing atmosphere
Miniaturized sample size
Oxidation

ABSTRACT

Hydrogen-containing atmospheres are of growing interest for high-temperature applications, but their influence on the creep behavior of Ni-based superalloys remains difficult to assess under realistic conditions. In this study, the creep response of Waspaloy was investigated using miniaturized tensile specimens and related to oxidation behavior in Ar and Ar + 5 % H_2 atmospheres. The applicability of the miniaturized creep approach was first assessed by comparison with conventional macroscopic specimens. At 925 °C and 120 MPa, macro and micro specimens showed broadly similar creep behavior during the short test durations, indicating that surface-related degradation did not dominate the overall response. At 875 °C and 80 MPa, the minimum creep rates remained similar in both atmospheres, whereas subsequent creep softening was delayed in Ar + 5 % H_2. Complementary oxidation experiments at 875 °C revealed a thicker, more heterogeneous oxide scale with stronger internal oxidation in Ar, while Ar + 5 % H_2 produced a thinner, more homogeneous oxide scale. These results show that the creep response of miniaturized specimens is strongly influenced by oxidation-induced surface degradation and the resulting reduction of the effective load-bearing cross section. A direct hydrogen effect on the high-temperature creep mechanism could not be conclusively identified.

1. Motivation

To address ambitious climate targets, hydrogen is considered as a promising alternative fuel. In recent years, its potential for use in aviation and stationary gas turbines has been increasingly recognized as a compelling option [1–5]. For example, when hydrogen is used as a fuel in aircraft, turbine materials may be exposed to hydrogen before combustion to H_2O. In addition, incomplete combustion or reactions of water with Ni_3Al on hot metal surfaces can lead to catalytic hydrogen regeneration or alumina formation accompanied by hydrogen release [6]. This introduces the risk of hydrogen embrittlement [7], a phenomenon that has been extensively studied in recent decades and several hydrogen embrittlement mechanisms have been proposed [8–10]. Especially in gas turbines, where Ni-based superalloy are usually used in the hottest sections, materials should exhibit high resistance to hydrogen. Research on hydrogen embrittlement in superalloys so far is mainly focused on the widely used polycrystalline superalloy Alloy 718. It was found that a higher fraction of the different precipitation phases leads to a higher hydrogen susceptibility [11–15]. The applications of Alloy 718 extend beyond gas turbines, being crucial in the oil and gas industry, particularly in drilling deep wells for oil extraction, where hydrogen embrittlement is a significant concern [16]. Studies have also identified that the δ phase, which acts as grain boundary pinning phase, has the most detrimental effect on hydrogen embrittlement [12]. Additionaly, research conducted by Botinha et al. [17] has shown that higher volume fractions of γ' precipitates and/or lower volume fractions of γ''precipitates have positive effects on the material's resistance to hydrogen embrittlement. In contrast to that, our previous studies on different alloys demonstrated that γ' precipitates have a significant impact on hydrogen embrittlement and that the γ' phase accumulates hydrogen [18,19].

The classical approach to study hydrogen-induced effects, is to first introduce hydrogen into the material using different charging methods, and then to examine the potential effects. So far, this has primarily been accomplished through ex-situ charging methods, either electrochemically or using gaseous hydrogen, the latter of which entails significantly

---

* Corresponding author.
E-mail address: oliver.nagel@fau.de (O. Nagel).

https://doi.org/10.1016/j.matdes.2026.116020
Received 27 February 2026; Received in revised form 9 April 2026; Accepted 13 April 2026

stricter safety regulations [20]. Gaseous charging offers key advantages, such as avoiding additional corrosion effects and enabling higher charging temperatures. This is especially critical for face-centered cubic alloys, which have significantly slower hydrogen diffusion rates than body-centered cubic materials, especially at lower temperatures [21]. However, a significant gap remains in the implementation of in-situ hydrogen charging at high temperatures, which is essential for studying superalloys under realistic turbine operating conditions, where the material can be exposed to unburned hydrogen from the exhaust. The main challenge in performing in-situ tests in a hydrogen atmosphere at elevated temperatures is the strict safety requirements. Schulz et al. [22] proposed a novel experimental approach based on direct flame exposure, where specimens were exposed directly to a hydrogen flame to mimic combustion conditions.

Another viable alternative is the use of forming gas, a mixture of argon with 5 % hydrogen (Ar + 5 % H_2), which also can mimic possible hydrogen concentrations in the exhaust. So far, only a few publications have reported a degradation of creep life in hydrogen atmospheres for austenitic steels [23], Ni-rich binary Fe-Ni alloys [24] and several Ni-based superalloys at elevated temperatures [25,26].

As superalloys are used at high temperatures, not only the creep resistance, but also the oxidation behaviour becomes critical. Although the reducing nature of hydrogen [27] generally leads to lower oxidation rates, various thermodynamic driving forces may still influence the formation and stability of a protective oxide scale. Moreover, hydrogen combustion significantly increases the water vapour content in the environment. It has been reported that water can react with chromia (Cr_2O_3), promoting the breakdown of the protective oxide layer [28]. In addition, water vapor enhances the outward diffusion of metal cations, resulting in the formation of coarser and less adherent oxide scales [29]. Therefore, a thorough understanding of the oxidation behaviour of superalloys in hydrogen-containing atmospheres and water vapor is necessary to assess their suitability for potential hydrogen-fuel applications.

In the present study, miniaturized tensile specimens were tested in hydrogen-free and hydrogen-containing atmospheres using a thermomechanical analyzer (TMA) to investigate the influence of hydrogen on creep and oxidation as a first step. Tensile creep tests on microscopic specimens in the TMA have previously been successfully conducted at our institute on bond coats [30,31]. In comparison to other studies using miniaturized tensile specimens [32–34], the creep specimens of this study exhibited an even further reduced diameter of just 150 μm in the gauge length. This enabled well controlled testing in hydrogen-containing atmospheres within the TMA and studying the impact of differences in the oxidation behaviour in both atmospheres due to the high surface-to-volume ratio of such miniaturized samples which amplifies potential surface effects due to oxidation.

The aim of this study was therefore twofold. First, the applicability of miniaturized creep specimens for investigating the creep response of Waspaloy was assessed by comparison with conventional macroscopic specimens. Second, the creep behavior of miniaturized specimens in Ar and Ar + 5 % H_2 atmospheres was investigated and related to the corresponding oxidation behavior under otherwise comparable thermal exposure conditions. In the present work, the focus is therefore not on isolating a pure hydrogen effect, but on assessing the overall material response in a hydrogen-containing atmosphere under the residual-oxygen conditions of the experimental setup.

2. Methods and material

To investigate the influence of the specimen size, creep tests were carried out initially at 925 °C and 120 MPa using M10 threaded head specimens (macro samples) and microscopic samples (micro samples) of Waspaloy. A comparison of the specimen sizes is shown in Fig. 1 a) and an image at higher magnification of the micro sample is shown in Fig. 1 b). Due to the observed high creep rates, the testing parameters were subsequently adjusted to 875 °C and 80 MPa to achieve more representative creep experiments. The selected test temperatures are higher than the maximum technical application temperatures of Waspaloy in the range between ~ 650 °C and ~ 820 °C [35–38]. However, these comparatively high test temperatures are necessary because the maximum force or stress for carrying out the miniaturized creep tests in the TMA was specified as 3 N or ~ 170 MPa.

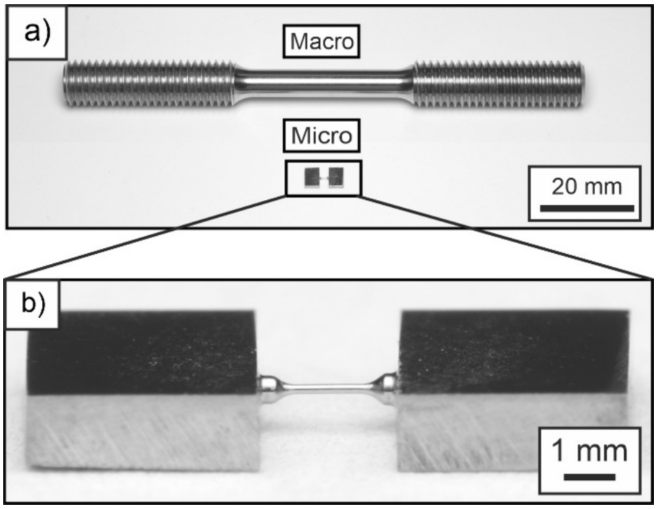

Fig. 1. In a) the sample dimensions for macro and micro specimens are compared and b) shows the micro sample at a higher magnification.

The macro specimens were produced by cutting cylinders from the sample material using wire erosion, followed by CNC milling to achieve the final geometry. The diameter within the gauge length of the macro specimen with M10 threaded head was 6 mm.The macro samples were tested in a universal testing machine Instron 4505 *(Instron GmbH, Darmstadt/ Germany*) in constant stress mode. To minimize the influence of thermal expansion effects at the beginning of the experiment, a dwell time of 1 h was maintained at the target temperature under a preload of 250 N. The micro samples were produced at the company *Microsample* (Scharnstein/Austria) from sample material platelets measuring 4 x 8 x 1.2 mm using a newly developed method [39]. A cylindrical grinding and polishing process is used, which leads to a high-precision sample geometry with no significant manufacturing-related influence zone on the sample surfaces. Final diameter within the gauge length was 150 μm for the micro tensile specimens. All creep experiments for the micro specimens were carried out in the TMA (Netzsch, Selb/Germany) in constant loading mode. For the creep tests a preload of 0.05 N was applied during the heating and holding process and an Ar gas flow of 100 ml/min was used in both the furnace chamber and the measuring system. Here, as well a holding time of 1 h at the test temperature was applied prior to the start of the creep test to minimize the effects of thermal expansion. The same procedure was repeated for the experiments conducted in a hydrogen-containing atmosphere, with the exception that Ar + 5 % H_2 was used instead of Ar. Since both the forming gas and the Ar gas contained trace amounts of O_2, the specimen surfaces oxidized during the creep experiments. In total, two experiments were performed for each combination of atmosphere, temperature, and stress condition for the micro samples and one experiment for the macro sample.

For a detailed investigation of oxidation in a Ar or Ar + 5 % H_2 atmosphere, both containing trace amounts of O_2, additional heat treatments in the TMA were perfomed without load on cubic samples with dimensions of 5 x 5 x 5 mm for 24, 48 and 96 h at 875 °C. In order to protect the oxide layer after heat treatment the samples are first wrapped with a thin Ag foil (~ 8 μm) and then further wrapped with Al foil (~ 50 μm) to safeguard the inner Ag layer. The samples are then hot-embedded and subsequently ground and polished for SEM examination.

A CrossBeam 1540EsB (*Zeiss AG*, Oberkochen/Germany) and a Helios NanoLab 600i (*FEI*, Hillsboro/USA) dual-beam device with electron beam and focused ion beam were used for analysis of initial microstructure and fractured crept samples. In the case of the CrossBeam 1540EsB, the acceleration voltage was 20 kV and the working distance was 8 mm for SE and 6 mm for BSE images. A 30 μm aperture was used for recordings in SE mode and a 120 μm aperture for recordings in BSE mode. In addition, EDS measurements were also carried out on this device to determine the chemical composition and EBSD measurements to obtain information on grain orientation and size. An INCA Energy 350 EDS detector and a Nordlys2 EBSD detector (*Oxford Instruments PLC*, Abingdon/United Kingdom) were used for this purpose. An acceleration voltage of 20 kV, a working distance of 8 mm and a 30 μm aperture were selected for the EDS measurements. The INCA software (*Oxford Instruments PLC*, Abingdon/United Kingdom) was used to evaluate the EDS measurements. The EBSD measurements were carried out on a sample holder tilted forward by 70° at an acceleration voltage of 20 kV, but with a working distance of 16 mm and a 120 μm aperture. The EBSD measurements were evaluated using the AzTecCrystal software (*Oxford Instruments PLC*, Abingdon/United Kingdom). In the case of the Helios NanoLab 600i, the working distance was 4 mm with an acceleration voltage of 10 kV. Acquired images were evaluated by Fiji distribution of ImageJ software [40] for the determination of the volume fraction and the size of the γ' precipitates. Machine learning based Trainable Weka Segmentation plugin for Fiji was used [41].

Phase identification of the alloys after exposure was conducted using X-ray diffraction (XRD) with a Seifert PAD II diffractometer. Measurements were performed in Bragg–Brentano geometry (θ–2θ), utilizing Cu $K\alpha_1$ radiation ($\lambda = 0.15406$ nm), with a step size of 0.01° and a scan rate of 1°/min.

Depth profiling was conducted on two selected samples after 24 h exposure using Auger Electron Spectroscopy (AES, PHI 710e / 680 Hybrid Auger Nanoprobe). An argon ion beam with an acceleration voltage of 3 kV and an ion current of 3 μA was employed as the sputtering source.

Surface morphology, cross-sectional structure, and elemental distribution for oxidized samples were analyzed by scanning electron microscopy (SEM, Philips XL30S and JEOL JSM6400) equipped with energy-dispersive X-ray spectroscopy (EDS). For cross-sectional observations, samples were mounted in epoxy, ground with SiC papers, and polished using diamond suspensions. Quantitative analysis of the oxide scale thickness, including delineation of individual sublayers, as well as the determination of internal oxidation regions was performed using SEM images and evaluated again with ImageJ software. For the determination of the γ'-depleted region, the average of the three longest cracks was evaluated for each of the four sides of the cube. In this context, it was assumed that the length of cracks along grain boundaries or oxidized grain boundaries corresponds to the extent of the γ'-depleted zone (internal oxidation region).

Furthermore, hot gas extraction for quantification of hydrogen content was performed with the device H-500 from the company *Eltra*. The measurement principle is the change of the thermal conductivity of a carrier gas by effusion of H (up to 1000 °C). This was done with one cubic sample after heat treatment at 875 °C for 24 h in Ar or Ar + 5 % H_2 atmosphere. This study was perfomed on the polycrystalline Ni-based superalloy Waspaloy, which was already widely investigated in literature regarding its creep properties [42–44]. Table 1 displays the chemical composition of Waspaloy, without mentioning any minor elements, e.g. C, Si, P or S. Measured quantities were carried out by EDS measurements and compared to the nominal composition. All experiments were done from the same batch on a fully heat-treated condition, which is commercially available.

Table 1
Nominal and measured (EDX) composition of Waspaloy in at. %.

Element	Ni	Cr	Co	Mo	Ti	Al
Measured / at. %	Bal.	22.5	13.1	2.7	3.7	2.7
Nominal / at. %	Bal.	21.3	13.0	2.5	3.6	2.7

The microstructure is shown in Fig. 2 a), c), and d) using BSE-SEM images at different magnifications, and in Fig. 2 b) using an EBSD scan at the same magnification as Fig. 2 a), which was used for the evaluation of the median grain size.

The polycrystalline structure has a mean grain size of 7.2 ± 6.1 μm. The spherical primary (Fig. 2 d)) and secondary γ' precipitates (see Fig. 2 c)) have an median diameter of a volume-equivalent sphere of 267 ± 63 nm and 47 ± 16 nm respectively. The γ' volume fraction determined from the BSE-SEM image is 33 %, which agrees well with literature values of 27 % − 33 % [45–47].

3. Results

In addition to comparing the macro and micro sample sizes, the creep performance of the Micro specimens in Ar and Ar + 5 % H_2 atmospheres is evaluated. Furthermore, the results of the detailed oxidation analysis at 875 °C are presented.

3.1. Validation of microscopic creep tests

The results of the tensile creep tests on the macro and micro samples are displayed for the testing parameters of 875 °C and 80 MPa (Fig. 3 a, c) and for 925 °C and 120 MPa (Fig. 3 b, d).

With the micro sample in particular, however, care should be taken to ensure that the size of the microstructure is not of the same order of magnitude as the sample diameter so that the mechanical properties are not influenced by, for example, the orientation of individual grains or very large volume of a phase [38,48–50]. In the case of Waspaloy, however, this is not the case with a ratio of the diameter of the microscopic sample to the median grain size of ~ 21. In Fig. 3 a) the creep properties of micro and macro samples is compared in a strain rate against true strain plot. It should be noted that this comparison is primarily intended to assess the general applicability of the miniaturized specimen geometry, since the macro specimens were tested in air whereas the micro specimens were tested in Ar or Ar + 5 % H_2. Therefore, differences between macro and micro specimens cannot be attributed solely to specimen size, as environmental effects, particularly oxidation, also contribute to the observed creep response.

Shortly after the creep stress is applied, a creep minimum is formed, followed by softening until fracture. The minimum creep rates of the different sample geometries are in very good agreement and fall within the range of typical specimen to specimen and measurement scatter, as shown in Fig. 6a. To further illustrate this, Fig. 3 a) presents a magnified view of the first 3 % plastic strain, highlighting the comparable minimum creep rates of both specimen sizes at 875 °C and 80 MPa.

Concerning the elongation at fracture, pronounced differences are observed. A certain degree of scatter between tests conducted under identical conditions is expected due to the sensitivity of creep deformation to local microstructural variations, particularly for the micro specimens. The most significant difference in creep behaviour is observed at 875 °C and 80 MPa, where the micro specimens exhibit a sharp minimum in the creep rate followed by rapid softening, whereas the macro specimens do not show such a sharp minimum. This behaviour is also reflected in the rapid increase in strain for the micro specimens, as shown in Fig. 3 c).

In contrast, at 925 °C and 120 MPa, the creep curves of macro and micro specimens are very similar in both representations − strain rate versus strain (Fig. 3 b)) and strain versus time (Fig. 3 d)) − with the exception of the earlier fracture observed for the micro specimens. These differences are attributed to surface-dominated degradation mechanisms, which become increasingly relevant for the micro specimens owing to their high surface-to-volume ratio. In macro specimens, deformation is distributed over a much larger volume, resulting in a

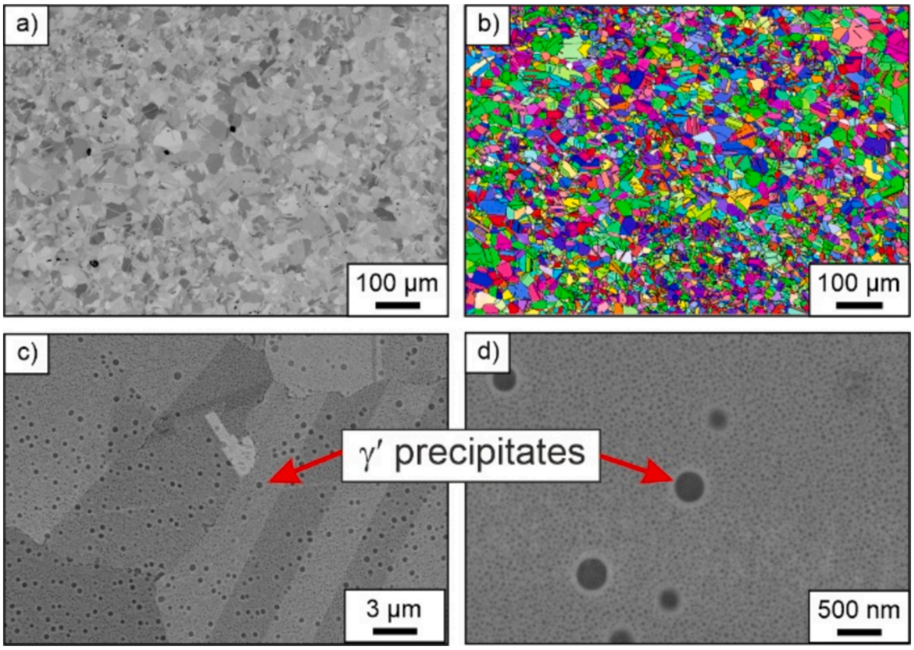

Fig. 2. Microstructure of Waspaloy at different magnifications is shown in a), c) and d). The IPF map of the EBSD measurement for grain size determination is displayed in b).

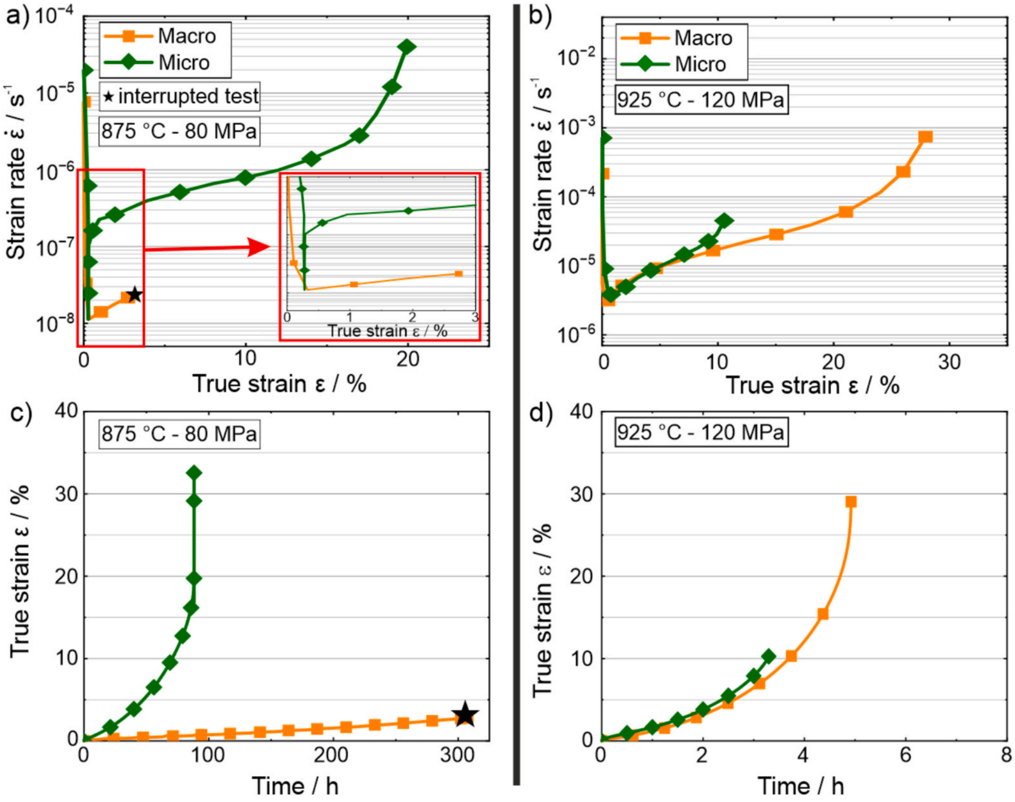

Fig. 3. Comparison of the creep performance of macroscopic and miniaturized specimens is presented in plots of strain rate versus strain at a) 875 °C and 80 MPa, and b) 925 °C and 120 MPa. Moreover, c) presents the plots of true strain versus time for 875 °C and 80 MPa and d) true strain against time for 925 °C and 120 MPa. Macro specimens were tested in air, whereas microscopic specimens were tested in Ar-based atmospheres. The comparison therefore serves primarily to assess the general applicability of the miniaturized approach rather than to isolate a pure specimen-size effect.

more gradual softening behaviour and a less pronounced minimum creep rate compared to the micro specimens. A detailed mechanistic discussion of these effects is provided in Chapter 4.

To gain further insight into the differences in elongation at fracture and the surface oxidation, longitudinal cuts of macro and micro specimens tested at 925 °C and 120 MPa were subsequently analyzed by SEM.

BSE-SEM images of the fractured specimens after the creep experiment at 925 °C and 120 MPa are presented in Fig. 4. The formation of

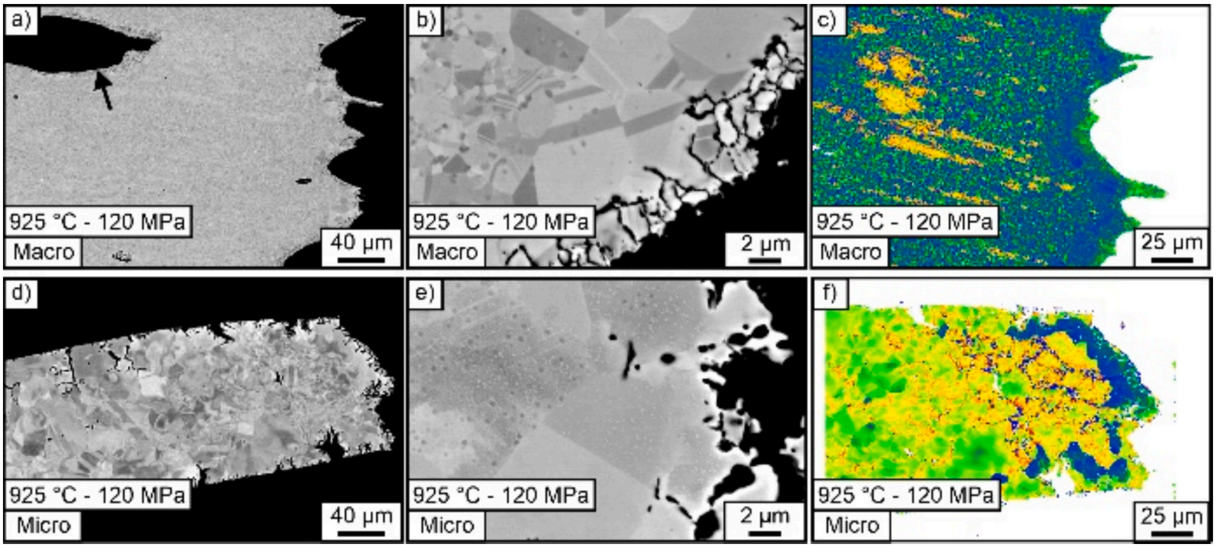

Fig. 4. BSE-SEM images of the fractured specimen after the creep test at 925 °C and 120 MPa are shown for a), b) the Macro specimen and d), e) the Micro specimen. Additionally, the local misorientation at the fracture surfaces is shown in c) for Macro and f) for Micro.

creep pores in the macro sample is visible in Fig. 4 a), which is marked by a black arrow. These creep pores lead to a reduction in the effective cross-section, resulting in a higher local stress and ultimately to failure of the specimens. Creep pores are caused by the accumulation of vacancies or dislocations at grain boundaries [48].

The absence of creep pore formation in the micro tensile specimen can be explained by the shorter test time and lower elongation at fracture. The shorter test duration is also reflected in the local misorientation maps obtained by EBSD (Fig. 4 c) and f)), which can be used as a qualitative measure of the dislocation density. A significantly lower dislocation density is observed in the macro specimens compared to the micro specimens. This difference can be attributed to dynamic recrystallization occurring during the more pronounced tertiary creep regime and the longer overall test duration in the macro-scale tests. As evident

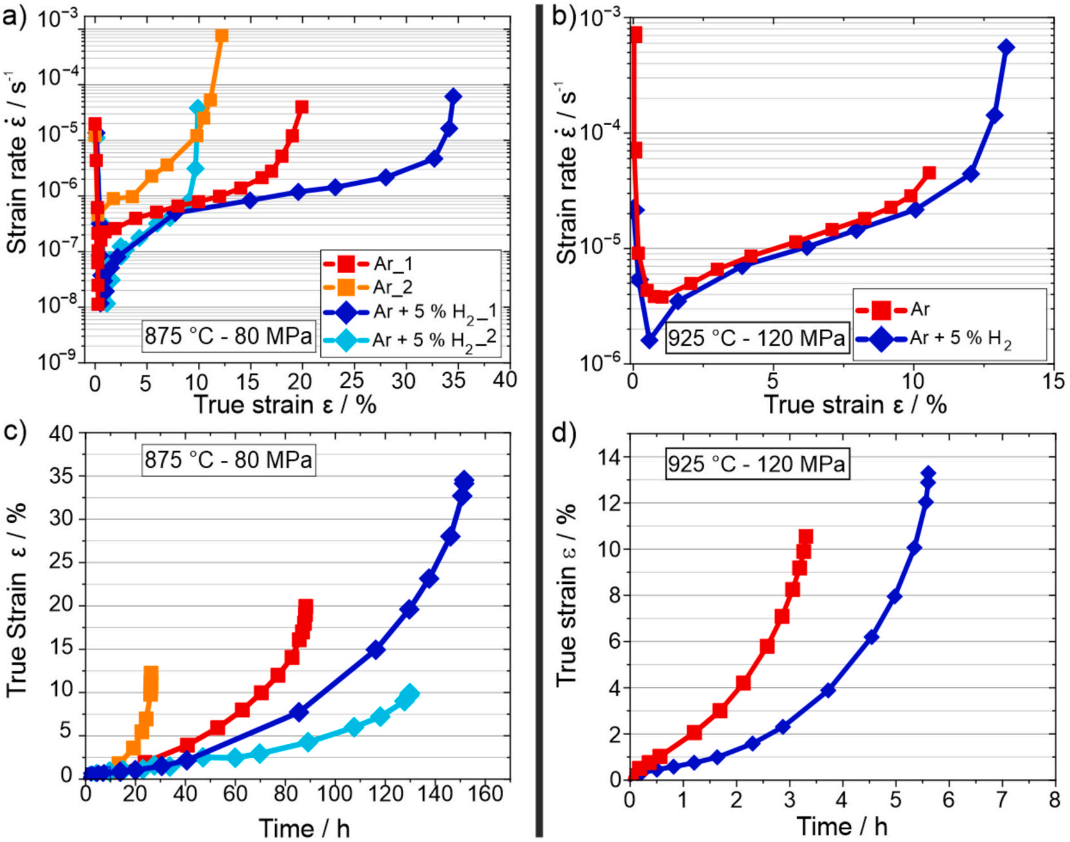

Fig. 5. Comparison of the creep performance of Micro specimens in Ar and Ar + 5 % H_2 atmosphere is presented in plots of strain rate versus strain at a) 875 °C and 80 MPa, and b) 925 °C and 120 MPa. Additionally, c) presents the plots of true strain versus time for 875 °C and 80 MPa and d) true strain against time for 925 °C and 120 MPa.

in Fig. 4 b), the high density of cracks reveals significant grain-boundary oxidation, which reduces the effective cross-section of the specimen and can ultimately lead to failure of the specimen. Such intergranular oxidation has also been found in the literature for Waspaloy at temperatures above 800 °C [38,44,51–53].

A similar phenomenon can also be seen directly on the fractured sample of the micro tensile specimen in Fig. 4 d) and e). Oxidation of the grain boundaries also occurs here, and no γ' precipitates are present in the adjacent region with reduced dislocation density. This γ' depleted zone is caused by Al and Ti segregation from the γ' precipitates to the grain boundaries to form Al_2O_3 and TiO_2 [52,53]. Owing to the small initial cross-section of the micro samples, surface oxidation may additionally influence the mechanical strength, since the reduction of the effective cross-section leads to an increase in the true stress level, which may explain the earlier fracture of the micro samples compared to the macro samples at 925 °C and 120 MPa.

3.2. *Creep performance in Ar + 5 % H_2 compared to Ar atmosphere*

Fig. 5 presents the results of the tensile creep tests for micro samples conducted in the TMA under Ar and Ar + 5 % H_2 atmospheres. Concerning the minimum strain rates for both specimen sizes and testing atmospheres, the minimum creep rates are very similar in all cases. The experiments conducted in an Ar + 5 % H_2 atmosphere exhibit even slightly lower minimum creep rates (Fig. 6 b)) and longer time to fracture, the latter contrasts with the commonly reported degradation of creep life in hydrogen-containing environments.

The elongation at fracture exhibits considerable scatter, with no systematic or consistent trend observed between the two atmospheres. Such scatter is expected for micro specimens due to their pronounced sensitivity to local microstructural variations and surface-related effects.

As anticipated, the creep rates at 925 °C and 120 MPa (Fig. 5b,d) are significantly higher than those measured at 875 °C and 80 MPa (Fig. 5a, c). This is evident in both the strain rate versus strain representation and the strain versus time curves, where the higher temperature and stress result in accelerated deformation and much shorter test durations.

In general, the micro specimens exhibit the characteristic stages of creep deformation. At 875 °C and 80 MPa, the creep curves show a pronounced minimum creep rate followed by accelerated softening, whereas at 925 °C and 120 MPa the transition from decreasing to increasing creep rate is more gradual because of the much shorter test duration. This is particularly evident in the strain rate against strain plots, where the increase in creep rate at higher strains occurs over a relatively narrow strain interval.

At 875 °C and 80 MPa, the creep curves consistently display a sharp minimum in creep rate, followed by a rapid increase in strain rate indicative of pronounced softening (Fig. 5 a)). This behaviour is also reflected in the strain versus time curves (Fig. 5 c)), where deformation accelerates markedly after the minimum creep rate has been reached. As discussed previously for the micro specimens in Fig. 3, this pronounced minimum and subsequent softening are characteristic of micro specimens tested under long-duration creep conditions and may be attributed to surface-dominated degradation mechanisms, such as oxidation-induced γ' depletion and the associated reduction of the mechanically effective cross section. However, the subsequent softening proceeds more slowly in Ar + 5 % H_2 than in pure Ar, which is also reflected by the earlier increase in strain observed in the Ar atmosphere (see Fig. 5 c)). This behaviour could be correlated with the reduced oxidation kinetics in the hydrogen-containing environment.

In contrast, the tests conducted at 925 °C and 120 MPa do not exhibit a distinct or sharp minimum in the creep rate (Fig. 5 b)). Instead, the creep rate decreases only briefly before transitioning into a more gradual acceleration toward tertiary creep. Owing to the significantly shorter test durations at these conditions (Fig. 5 d)), surface-related effects have less time to develop and therefore influence the creep response only at later stages of deformation, if at all. As a result, the creep curves at 925 °C and 120 MPa are comparatively similar for both atmospheres, with differences becoming apparent mainly in the final stages leading to fracture.

Nevertheless, it can be concluded that, for both specimen sizes and atmospheres, the creep curves obtained at 925 °C and 120 MPa exhibit very similar trends. In contrast, at 875 °C and 80 MPa, while the minimum creep rates remain comparable, the subsequent softening is less pronounced for micro specimens tested in Ar + 5 % H_2 compared to Ar, particularly at 875 °C and 80 MPa.

Still differences in surface oxidation between Ar and Ar + 5 % H_2 atmospheres are primarily expected to affect the total elongation at fracture. However, internal grain boundary oxidation and the associated γ' dissolution – due to the diffusion of γ'-forming elements such as Al and Ti to form oxides – may also influence the overall mechanical strength, potentially leading to variations in creep resistance. Owing to the significantly different test durations, the fractured samples were not further analysed. Instead, additional heat treatments without applied load were conducted for defined time intervals to investigate differences in oxidation behaviour between the two atmospheres.

3.3. *Oxidation behaviour*

To explain potential differences in the creep performance the oxidation behaviour in the two different atmospheres at 875 °C was analyzed on macroscopic samples without load.

The hydrogen concentration within the samples was determined to be 1.8 wt ppm after 24 h exposure to an Ar atmosphere and 5.9 wt ppm to Ar + 5 % $H_{2,}$ which means a slight hydrogen incorporation after heat treatment in Ar + 5 % H_2 can be detected.

EDS mappings on cross sections show the expected general oxidation behaviour for superalloys (see Fig. 7). Ti and Cr are enriched in the outer oxide layer, whereas Al mainly forms oxides along grain boundaries. As already mentioned, this oxidized region leads to a γ'-depleted zone, because the γ' forming elements Al und Ti are consumed for the oxide formation.

To gain further insight into the oxide layer, AES depth profiles and SEM cross-sectional images were obtained after 24 h of heat treatment (Fig. 8). These analyses were performed to provide a qualitative assessment of oxide composition and thickness. The SEM cross-sections in Fig. 8 show a clear contrast between two phases in the oxide scale in the case of pure Ar and a single layer for Ar + 5 % H_2. With the depth profiles in Fig. 8 it can be confirmed that in Ar atmosphere a thin top layer of TiO_2 with a sublayer of Cr_2O_3 develops, whereas a single layer of Cr-Ti oxide exists for the specimen oxidized in the Ar + 5 %H_2 atmosphere. Also the oxide layer in the hydrogen-containing atmosphere appears much more homogeneous, whereas the oxide layer in the case of the Ar atmosphere demonstrate a much higher roughness.

In Fig. 9 a) XRD patterns for 96 h heat treatment time at 875 °C in the two different atmospheres are displayed. Next to the marker peaks for Ni as the base element, characteristic peaks for Cr_2O_3 and TiO_2 are observable for the specimen oxidized in Ar atmosphere. Interestingly, for the Ar + 5 % H_2 atmosphere no TiO_2 peaks occur, instead peaks at different diffraction angles appear, which can be assigned to Cr_2TiO_5. In contrast, such Bragg peaks for Cr_2TiO_5 are not present in the sample tested in Ar atmosphere. Peaks for Cr_2O_3 are also observable for Ar + 5 % H_2, but strongly weakend compared to the Ar atmosphere. Also SEM images of the oxide surfaces after 96 h of heat treatment in Fig. 9 b) reveal notable differences in morphology. While in the hydrogen-containing atmosphere a quite flat surface can be detected with Cr-rich particles, the oxide layer in pure Ar consists of coarse grains, which are most likely TiO_2 grains, considering the absence of TiO_2 peaks in the case of Ar + 5 % H_2. This matches with the cross sections from Fig. 8, which showed a much higher roughness in the case of pure Ar atmosphere. Additionally, small reflections at approximately 37°, 45°, 57° and 67° are visible for Ar + 5 % H_2, which can be assigned to a chromite spinel ($NiCr_2O_4$) and are consistent with the chromium-rich

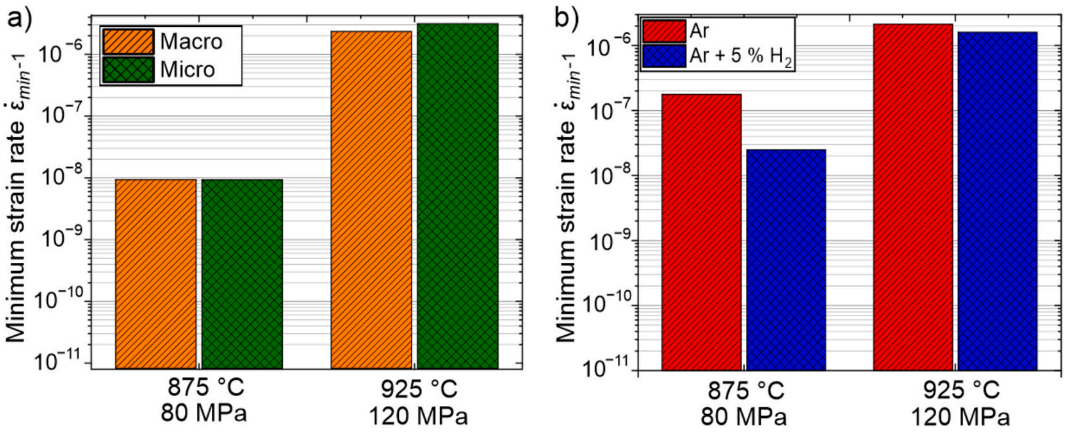

Fig. 6. A) bar chart presents the minimum strain rates for both testing conditions (875 °C/80 MPa and 925 °C and 120 MPa and specimen sizes (Macro and Micro) and in b) minimum strain rates are displayed for both testing conditions and atmospheres for the Micro samples.

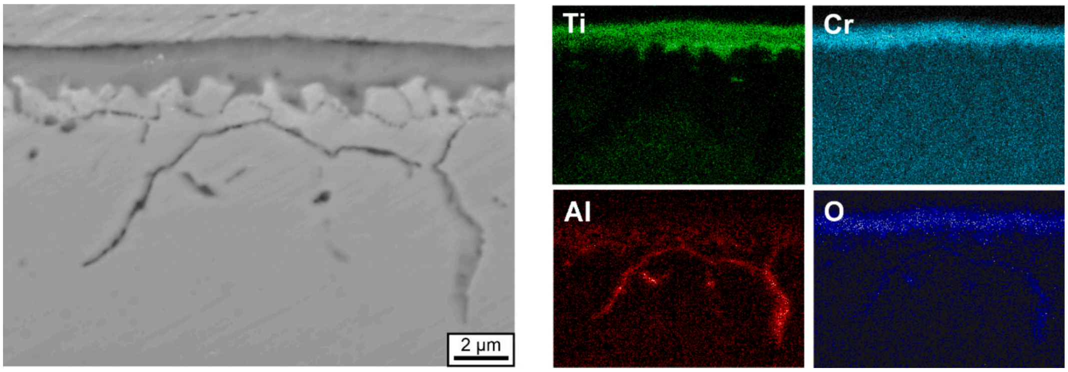

Fig. 7. Exemplary EDS mappings for Ti, Cr, Al and O, which were performed on the sample after heat treatment for 48 h in Ar + 5 % H_2.

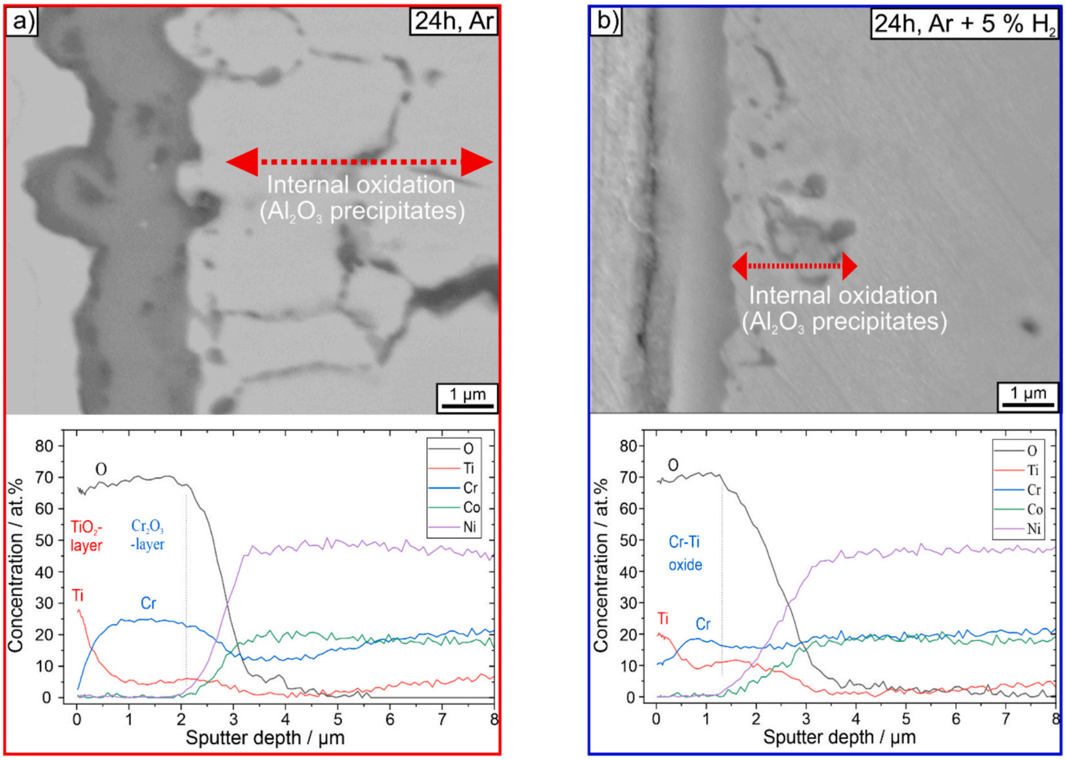

Fig. 8. Depth Profile measurements with corresponding in cross-section SEM micrographs in a) of 24 h heat-treated samples in Ar and b) Ar + 5 % H_2 atmosphere.

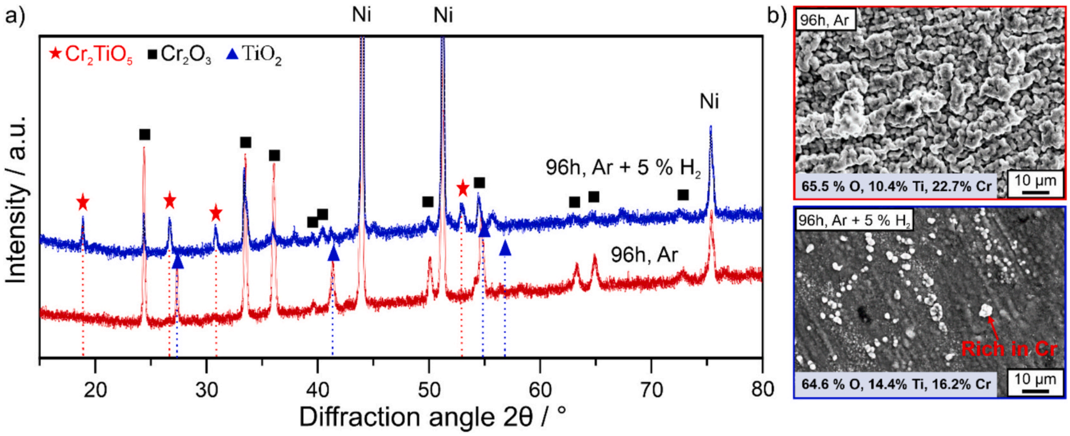

Fig. 9. In a) lab-XRD patterns of all heat treated conditions are showen, which reveal different oxide composition in the two atmospheres. Additional SEM images in b) of the 96 h heat-treated conditions at 875 °C in Ar and Ar + 5 % H_2 atmosphere demonstrate significant differences in oxide surface morphology.

particles observed on the surface (see Fig. 9 b)). However, a detailed phase identification of these minor oxides is beyond the scope of the present study and will not be discussed further.

Afterwards, the total oxide thickness of all heat treated samples was evaluated using their cross sections. Furthermore the depth of the internal Al_2O_3-oxidation was measured, which also could impact the strength of the material by dissolution of γ' precipitates to form Al_2O_3. At least for the Micro sample size with a large surface-to-volume fraction this could possible have a notable impact on the creep performance. Fig. 10 a) indicates that the oxide layer thickness is lower for Ar + 5 % H_2 after all heat treatment times. It is also observable that especially in the first 24 h the oxide growth is higher in the Ar atmosphere, but between 24 h and 96 h the two different atmospheres show quite similar oxide growth rates.

The same trend is visibile for the internal oxidation by Al_2O_3 in Fig. 10 b). The region with oxidized grain boundaries is larger in the specimen oxidized in Ar, and its growth is particularly pronounced during the first 24 h. Based on these values, the residual load-bearing cross section of hypothetical micro creep specimens can be estimated by accounting for the oxide scale thickness and the γ'-depleted region. This corresponds to an estimated stress increase of 24.6 % in Ar and 18.2 % in Ar + 5 % H_2 after 24 h. After 96 h, the estimated stress increase rises to 47.1 % in Ar and 38.4 % in Ar + 5 % H_2.

4. Discussion

The observed oxidation behaviour can be directly correlated with the creep response at 875 °C and 925 °C. It should be noted that the oxygen partial pressure in the present experiments was not directly controlled or measured and may dynamically change due to reactions such as $H_2 + ½ O_2 \rightarrow H_2O$. Therefore, the reported oxidation behaviour should be interpreted in a qualitative manner, although the comparative trends between the two atmospheres remain valid.

At 925 °C and 120 MPa, the creep rates are high, resulting in very short test durations of up to ~ 6h. “Under these conditions, oxidation cannot be considered negligible despite the short test duration; however, the rapid softening is likely dominated by accelerated γ' dissolution at this temperature, which is expected to proceed similarly in both atmospheres. This interpretation is further supported by the significantly lower equilibrium γ' volume fraction at 925 °C (14.5 %), compared to 33 % in the as-received condition, as calculated using Thermo-Calc (TCNI12).” Fig. 11 schematically illustrates the correlation between creep performance and surface oxidation under these conditions. Oxidation leads to the formation of a γ'-depleted region along the specimen surface. For macro specimens with a low surface-to-volume ratio, this γ'-depleted zone remains small relative to the total cross-sectional area and therefore has only a minor, or even negligible, effect on the overall mechanical strength.

In addition to surface oxidation, recovery mechanisms active at high temperatures play a key role in governing the creep response. At temperatures exceeding the maximum service temperature of Waspaloy (~650–820 °C [35–38]), also dynamic recrystallization acts as an efficient mechanism to reduce the dislocation density generated during creep deformation [38,48,54]. This effect is evident in the macro

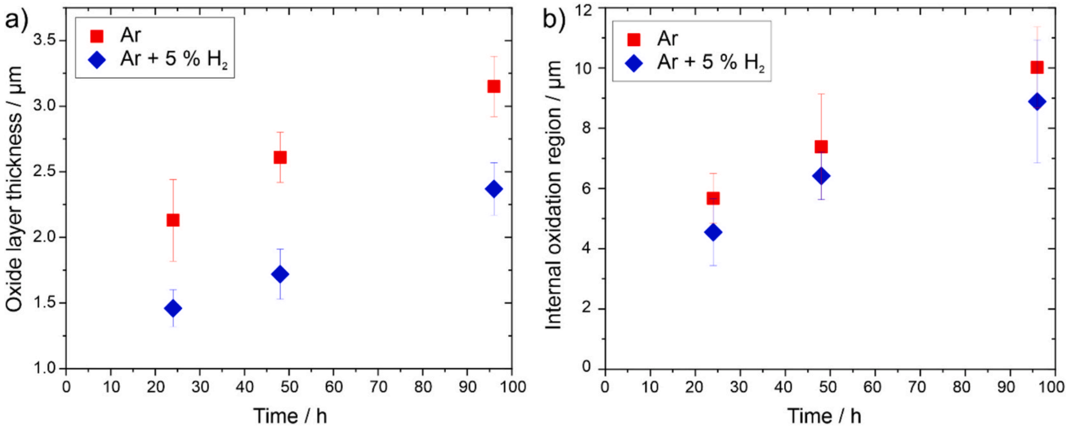

Fig. 10. Quantification of oxidation growth in the two different atmoshpheres at 875 °C, a) showing oxide layer thickness against heat treatment time and b) internal oxidation region versus heat treatment time. In this context, the internal oxidation region was assumed to be equivalent to the γ'-depleted zone.

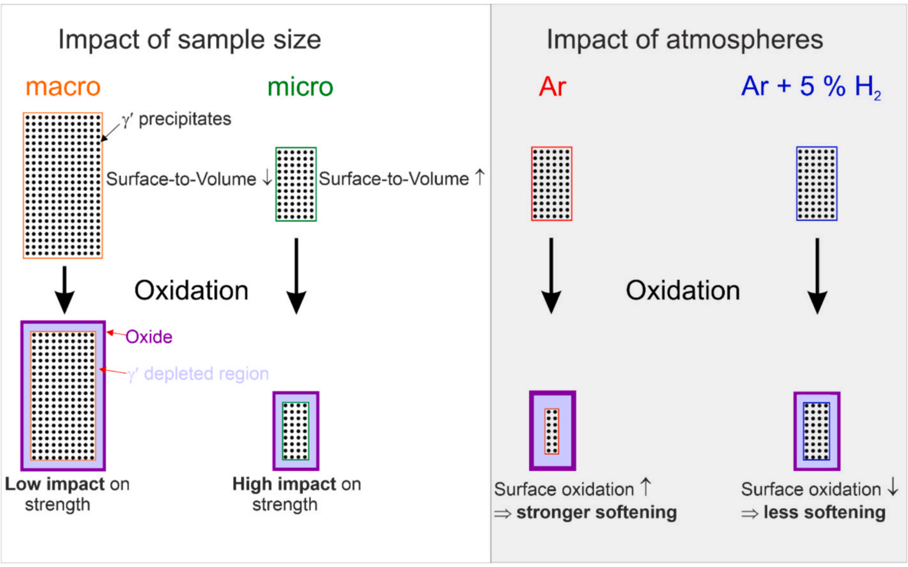

Fig. 11. Schematic depicting how surface oxidation affects mechanical strength and thereby creep resistance, highlighting the role of specimen size and testing atmosphere.

specimen tested at 925 °C and 120 MPa, as shown by the local misorientation map of the fracture surface (Fig. 4 c)). The higher elongation at fracture promotes dynamic recrystallization, which in turn leads to a reduction in the overall dislocation density.

The present results indicate that the creep response of miniaturized Waspaloy specimens is strongly influenced by oxidation-induced surface degradation. Owing to the high surface-to-volume ratio of the miniaturized specimens, oxide growth and the associated γ' depletion near the surface lead to a progressive reduction of the effective load-bearing cross section, thereby promoting creep softening. At 875 °C and 80 MPa, the longer exposure times allow this effect to become mechanically significant. Since oxidation proceeds more slowly in Ar + 5 % H_2 under the present conditions, degradation of the effective cross section is also delayed, which is consistent with the later onset of pronounced creep softening in this atmosphere.

The present study does not provide conclusive evidence for a direct hydrogen-induced change in the high-temperature creep mechanism of Waspaloy. Although a higher total hydrogen content was measured after exposure to Ar + 5 % H_2, neither the hydrogen distribution within the material nor its evolution during creep was determined. Consequently, hydrogen-related effects cannot be fully excluded, but they cannot be isolated from the simultaneously altered oxidation conditions in the present experiments. The observed differences in creep behavior should therefore be interpreted as the net result of deformation in different environmental conditions, with oxidation representing the dominant and directly supported mechanism in the present dataset.

In our study, where a residual oxygen partial pressure was present, a particularly rapid oxide growth was observed during the first 24 h. This led to an initially fast formation of rutile TiO_2 in Ar, whereas the reduced oxygen partial pressure in the hydrogen-containing atmosphere promoted a more simultaneous oxidation of Ti and Cr. Similar behaviour has been reported for Co–Ni-based superalloys, where improved oxidation resistance at 900 °C was attributed to an increased Ti content, as a continuous TiO_2 layer facilitates the formation of a compact and dense Cr_2O_3 sublayer [55]. This mechanism is in good agreement with the oxidation results observed for Waspaloy in Ar, which likewise contains high amounts of Co and Ti.

Concerning the chemical composition of the oxide layers formed in the two atmospheres, it is also worth noting that Li et al. [56] recently reported the formation of a Cr_2TiO_5 oxide layer on a Cr-based coating with elevated Ti content when exposed to a water–vapor atmosphere at high temperatures. The development of this mixed oxide was shown to substantially enhance the oxidation resistance of the coating. This has been attributed to the lower oxygen diffusivity in Cr_2TiO_5 compared to Cr_2O_3. Moreover, in that study, a bilayer consisting of Cr_2TiO_5 and Cr_2O_3 was observed, and the coherent interface between the two phases led to reduced oxidative stresses and improved adhesion of the oxide layer to the substrate.

In our investigation, the formation of the complex oxide Cr_2TiO_5 was also observed in an Ar + 5 % H_2 atmosphere, which exhibited enhanced oxidation resistance. The formation of Cr_2TiO_5 can be rationalized by the solid-state reaction between Cr_2O_3 and TiO_2 (rutile):

$Cr_2O_3 + TiO_2 = Cr_2TiO_5$.

As a simple estimation of the stability of the different oxides, their formation energies can be considered. These are reported as − 2.367 eV/atom for Cr_2O_3 [57], −3.092 eV/atom for Cr_2TiO_5 [58] and − 3.464 eV/atom for TiO_2 (rutile) [59]. Based on these values, the relative stability of the oxides can be expected to follow the order:

$TiO_2 > Cr_2TiO_5 > Cr_2O_3$.

Thus, TiO_2 should be the most stable oxide and is expected to form preferentially during the initial stages of oxidation. In addition, TiO_2 is well known to exhibit a high growth rate and poor protectiveness at elevated temperatures due to rapid cation diffusion [60–62].

In atmospheres with higher oxygen availability, such as air or residual-oxygen-containing Ar here, both thermodynamic and kinetic factors endorse the rapid formation of a TiO_2-dominated surface scale initially, with Cr-rich oxides subsequently developing beneath the TiO_2 layer. Similar scale architectures, consisting of an outer TiO_2 layer and an underlying Cr-rich oxide, have been frequently reported for Ni-based superalloys containing Ti and Cr [51,63,64]. In contrast, the reduced oxygen potential in the Ar + 5 % H_2 atmosphere suppresses the preferential growth of TiO_2 and promotes simultaneous oxidation of Ti and Cr, consistent with observations reported by Li et al. [56] for oxidation in steam. Under these conditions, TiO_2 and Cr_2O_3 readily react to form the complex oxide Cr_2TiO_5. The formation of this complex oxide effectively inhibits the growth of the poorly protective TiO_2 surface layer and reduces oxygen diffusivity through the scale, thereby decreasing the overall oxidation rate and improving scale protectiveness. Our results could indicate that oxidation resistance in hydrogen-containing and water steam atmosphere can be improved by a higher Ti content of the material.

5. Conclusion

This study investigated the creep and oxidation behavior of the Ni-based superalloy Waspaloy in Ar and Ar + 5 % H_2 using miniaturized creep specimens and complementary oxidation experiments. A direct effect of hydrogen on the creep mechanism could not be conclusively identified in the present study and should be addressed in future work using experiments with better-controlled oxygen potential and more detailed post-creep characterization. However, several important aspects were identified, and the main results are as follows:

- The comparison with macroscopic specimens showed that the miniaturized specimens reproduce the general creep response reasonably well, while being considerably more sensitive to surface-related degradation because of their high surface-to-volume ratio.
- At 925 °C and 120 MPa, the creep curves obtained in the two atmospheres were broadly similar, which is attributed to the short test duration and the dominant influence of rapid high-temperature softening.
- At 875 °C and 80 MPa, the minimum creep rates remained similar in both atmospheres, but the subsequent softening was delayed in Ar + 5 % H_2.
- Oxidation experiments at 875 °C showed a thicker and more heterogeneous oxide scale with stronger internal oxidation in Ar, whereas Ar + 5 % H_2 resulted in a thinner and more homogeneous oxide scale.These results show that, under the present residual-oxygen conditions, the differences in creep softening are closely related to differences in oxidation behavior and the resulting reduction of the effective load-bearing cross section in miniaturized specimens. specimns.

CRediT authorship contribution statement

O. Nagel: Writing – review & editing, Writing – original draft, Visualization, Methodology, Investigation, Formal analysis, Data curation, Conceptualization. **C. Tang:** Writing – review & editing, Visualization, Validation, Methodology, Investigation, Formal analysis. **L. Haußmann:** Writing – review & editing, Visualization, Validation, Methodology, Investigation. **A. Demirci:** Investigation. **S. Vollath:** Investigation. **M. Fritton:** Writing – review & editing, Validation, Investigation. **R. Gilles:** Writing – review & editing, Validation, Supervision, Resources, Project administration, Funding acquisition. **M. Göken:** Writing – review & editing, Validation, Supervision, Resources, Project administration, Funding acquisition. **B. Gorr:** Writing – review & editing, Validation, Resources, Project administration, Funding acquisition. **S. Neumeier:** Writing – review & editing, Visualization, Validation, Supervision, Resources, Project administration, Methodology, Funding acquisition.

Declaration of competing interest

The authors declare that they have no known competing financial interests or personal relationships that could have appeared to influence the work reported in this paper.

Acknowledgments

The authors acknowledge the financial support received from the Federal Ministry of Research, Technology and Space for the project 05K2022 entitled “An apparatus to study the influence of hydrogen charging and discharging on industrial developed and applied alloys–H2Mat“(grant numbers: 05K22WE1 & 05K22WO3). Furthermore, the authors gratefully acknowledge funding by the Deutsche Forschungsgemeinschaft (DFG) through projects A6 of the Collaborative Research Centre SFB/TR 103 “From Atoms to Turbine Blades – a Scientific Approach for Developing the Next Generation of Single Crystal Superalloys” and lastly special thanks to Bianca Grandjean and Leon Sutanto for their laboratory work and image analysis. The authors also thank Tobias Weingärtner from Karlsruhe Institute of Technology (KIT) for the AES measurements.

Declaration of generative AI in scientific writing

During the preparation of this manuscript, ChatGPT was used solely for language correction. After using this tool/service, the author(s) reviewed and edited the content as needed and take(s) full responsibility for the content of the published article.

Data availability

Data will be made available on request.

References

[1] S. Bruce, M. Temminghoff, J. Hayward, D. Palfreyman, Opportunities for hydrogen in aviation, CSIRO (2020).

[2] Clean Skies for Tomorrow: Sustainable Aviation Fuels as a Pathway to Net-Zero Aviation, World Economic Forum (2020).

[3] International Energy Agency, The Future of Hydrogen: Seizing today’s opportunities, OECD, 2019. https://doi.org/10.1787/1e0514c4-en.

[4] F. Ueckerdt, C. Bauer, A. Dirnaichner, J. Everall, R. Sacchi, G. Luderer, Potential and risks of hydrogen-based e-fuels in climate change mitigation, Nat. Clim. Chang. 11 (2021) 384–393, https://doi.org/10.1038/s41558-021-01032-7.

[5] H. Zhou, J. Xue, H. Gao, N. Ma, Hydrogen-fueled gas turbines in future energy system, Int. J. Hydrogen Energy 64 (2024) 569–582, https://doi.org/10.1016/j.ijhydene.2024.03.327.

[6] E.P. George, C.T. Liu, H. Lin, D.P. Pope, Environmental embrittlement and other causes of brittle grain boundary fracture in Ni3Al, Mater. Sci. Eng. A 192–193 (1995) 277–288, https://doi.org/10.1016/0921-5093(94)03236-X.

[7] W.H. Johnson, On some Remarkable changes Produced in Iron and Steel by the Action of Hydrogen and Acids, Nature 11 (1875) 393, https://doi.org/10.1038/011393a0.

[8] C.D. Beachem, A new model for hydrogen-assisted cracking (hydrogen “embrittlement”), Metall Trans 3 (1972) 441–455, https://doi.org/10.1007/BF02642048.

[9] L.B. Pfeil, The effect of occluded hydrogen on the tensile strength of iron, Proc. R. Soc. Lond. A 112 (1926) 182–195, https://doi.org/10.1098/rspa.1926.0103.

[10] S.P. Lynch, Environmentally assisted cracking: overview of evidence for an adsorption-induced localised-slip process, Acta Metall. 36 (1988) 2639–2661, https://doi.org/10.1016/0001-6160(88)90113-7.

[11] M.C. Rezende, L.S. Araujo, S.B. Gabriel, D.S. dos Santos, L.H. de Almeida, Hydrogen embrittlement in nickel-based superalloy 718: Relationship between $\gamma' + \gamma''$ precipitation and the fracture mode, Int. J. Hydrogen Energy 40 (2015) 17075–17083, https://doi.org/10.1016/j.ijhydene.2015.07.053.

[12] L. Liu, K. Tanaka, A. Hirose, K. Kobayashi, Effects of precipitation phases on the hydrogen embrittlement sensitivity of Inconel 718, Sci. Technol. Adv. Mater. 3 (2002) 335–344, https://doi.org/10.1016/S1468-6996(02)00039-6.

[13] F. Galliano, E. Andrieu, C. Blanc, J.-M. Cloue, D. Connetable, G. Odemer, Effect of trapping and temperature on the hydrogen embrittlement susceptibility of alloy 718, Mater. Sci. Eng. A 611 (2014) 370–382, https://doi.org/10.1016/j.msea.2014.06.015.

[14] Z. Tarzimoghadam, D. Ponge, J. Klöwer, D. Raabe, Hydrogen-assisted failure in Ni-based superalloy 718 studied under in situ hydrogen charging: the role of localized deformation in crack propagation, Acta Mater. 128 (2017) 365–374, https://doi.org/10.1016/j.actamat.2017.02.059.

[15] B. Dutta, M. Ajay Krishnan, V.S. Raja, Role of precipitation on the hydrogen embrittlement behavior of IN 718, Trans. Indian Inst. Met. 74 (2021) 223–233, https://doi.org/10.1007/s12666-020-02136-y.

[16] M. Ziomek-Moroz, Environmentally assisted cracking of drill pipes in deep drilling oil and natural gas wells, J. of Materi Eng and Perform 21 (2012) 1061–1069, https://doi.org/10.1007/s11665-011-9956-6.

[17] J. Botinha, H. Alves, C. Solís, H.M.-L. Zentrum, A. Feoktystov, B. Gehrmann, V. Baran, F.H. Maier-Leibnitz, Study of phase distribution on Alloy UNS N07718 in different hardening conditions and its relationship with hydrogen embrittlement susceptibility, (n.d.).

[18] O. Nagel, M. Fritton, A. Mutschke, M. Spörlein, A. Stark, D. Sheptyakov, C. Höschen, P. Felfer, R. Gilles, S. Neumeier, Impact of high-pressure hydrogen charging on mechanical behavior and lattice parameters of a polycrystalline CoNiCr-based superalloy, Scr. Mater. 260 (2025) 116594, https://doi.org/10.1016/j.scriptamat.2025.116594.

[19] M. Fritton, A. Mutschke, O. Nagel, A. Stark, M. Hafez-Haghighat, B. Gehrmann, S. Neumeier, R. Gilles, Influence of hydrogen on the γ-matrix lattice parameters of a Ni-based superalloy – a synchrotron diffraction study, J. Alloy. Compd. 1014 (2025) 178693, https://doi.org/10.1016/j.jallcom.2025.178693.

[20] G.B. Rawls, T. Adams, N.L. Newhouse, Hydrogen production and containment, in: Gaseous Hydrogen Embrittlement of Materials in Energy Technologies, Elsevier, 2012: pp. 3–50. https://doi.org/10.1533/9780857093899.1.3.

[21] Y. He, Y. Li, C. Chen, H. Yu, Diffusion coefficient of hydrogen interstitial atom in α-Fe, γ-Fe and ε-Fe crystals by first-principle calculations, Int. J. Hydrogen Energy 42 (2017) 27438–27445, https://doi.org/10.1016/j.ijhydene.2017.08.212.

[22] P. Schulz, D. Dziedzic, N. Rocha, C. Ezenwajiaku, M. Talibi, R. Balachandran, E. Galindo-Nava, Hydrogen uptake and embrittlement in nickel-base superalloys during hydrogen flame charging, Commun Mater 6 (2025) 265, https://doi.org/10.1038/s43246-025-00988-9.

[23] D. Takazaki, T. Tsuchiyama, R. Komoda, M. Dadfarnia, B.P. Somerday, P. Sofronis, M. Kubota, Effect of hydrogen on creep properties of SUS304 austenitic stainless steel, Corrosion 77 (2021) 256–265, https://doi.org/10.5006/3678.

[24] G.B.A. Schuster, R.A. Yeske, C.J. Altstetter, The effects of hydrogen on the creep rupture properties of fe-ni alloys, Metall. Trans. A 11 (1980) 1657–1664, https://doi.org/10.1007/BF02660520.

[25] J. Harris Jr, M. VanWanderham, Properties of materials in high pressure hydrogen at cryogenic, room, and elevated temperatures, Pratt&whitney Aircraft (1973).

[26] Jonathan A. Lee, Hydrogen Embrittlement, NASA Aeronautics and Space Administration (2016). NASA/TM-2016–218602.

[27] S. Luidold, H. Antrekowitsch, Hydrogen as a reducing agent: State-of-the-art science and technology, JOM 59 (2007) 20–26, https://doi.org/10.1007/s11837-007-0072-x.

[28] B. Pint, S. Dryepondt, K. Unocic, Oxidation of Superalloys in Extreme Environments. 7th International Symposium on Superalloy 718 and Derivates, 2010.

[29] S.R.J. Saunders, M. Monteiro, F. Rizzo, The oxidation behaviour of metals and alloys at high temperatures in atmospheres containing water vapour: a review, Prog. Mater Sci. 53 (2008) 775–837, https://doi.org/10.1016/j.pmatsci.2007.11.001.

[30] S. Giese, S. Neumeier, D. Amberger-Matschkal, J. Bergholz, R. Vaßen, M. Göken, Microtensile creep testing of freestanding MCrAlY bond coats, J. Mater. Res. 34 (2019) 2643–2652, https://doi.org/10.1557/jmr.2019.169.

[31] S. Giese, S. Neumeier, J. Bergholz, D. Naumenko, W.J. Quadakkers, R. Vaßen, M. Göken, Influence of different annealing atmospheres on the mechanical properties of freestanding MCrAlY bond coats investigated by micro-tensile creep tests, Metals 9 (2019) 692, https://doi.org/10.3390/met9060692.

[32] L. Luan, H. Riesch-Oppermann, M. Heilmaier, Tensile creep of miniaturized specimens, J. Mater. Res. 32 (2017) 4563–4572, https://doi.org/10.1557/jmr.2017.414.

[33] G. Mälzer, R.W. Hayes, T. Mack, G. Eggeler, Miniature specimen assessment of creep of the single-crystal superalloy LEK 94 in the 1000 °C temperature range, Metall. Mater. Trans. A 38 (2007) 314–327, https://doi.org/10.1007/s11661-006-9007-3.

[34] P. Wollgramm, D. Bürger, A.B. Parsa, K. Neuking, G. Eggeler, The effect of stress, temperature and loading direction on the creep behaviour of Ni-base single crystal superalloy miniature tensile specimens, Mater. High Temp. 33 (2016) 346–360, https://doi.org/10.1080/09603409.2016.1186414.

[35] J. Wosik, B. Dubiel, A. Kruk, H.-J. Penkalla, F. Schubert, A. Czyrska-Filemonowicz, Stereological estimation of microstructural parameters of nickel-based superalloy Waspaloy using TEM methods, Mater Charact 46 (2001) 119–123, https://doi.org/10.1016/S1044-5803(01)00112-7.

[36] L.M. Pike, Development of a Fabricable Gamma-Prime (γ') Strengthened Superalloy, in: Superalloys 2008 (Eleventh International Symposium), TMS, 2008: pp. 191–200. https://doi.org/10.7449/2008/Superalloys_2008_191_200.

[37] S. Gialanella, A. Malandruccolo, Aerospace Alloys, Springer International Publishing, Cham (2020), https://doi.org/10.1007/978-3-030-24440-8.

[38] M.J. Donachie, S.J. Donachie, Superalloys: A Technical Guide, 2nd ed., ASM International, 2002. https://doi.org/10.31399/asm.tb.stg2.9781627082679.

[39] G.B. Rathmayr, A. Bachmaier, R. Pippan, Development of a new testing procedure for performing tensile tests on specimens with sub-millimetre dimensions, J. Test. Eval. 41 (2013) 635–646, https://doi.org/10.1520/JTE20120175.

[40] J. Schindelin, I. Arganda-Carreras, E. Frise, V. Kaynig, M. Longair, T. Pietzsch, S. Preibisch, C. Rueden, S. Saalfeld, B. Schmid, J.-Y. Tinevez, D.J. White, V. Hartenstein, K. Eliceiri, P. Tomancak, A. Cardona, Fiji: an open-source platform for biological-image analysis, Nat. Methods 9 (2012) 676–682, https://doi.org/10.1038/nmeth.2019.

[41] I. Arganda-Carreras, V. Kaynig, C. Rueden, K.W. Eliceiri, J. Schindelin, A. Cardona, H. Sebastian Seung, Trainable Weka Segmentation: a machine learning tool for microscopy pixel classification, Bioinformatics 33 (2017) 2424–2426, https://doi.org/10.1093/bioinformatics/btx180.

[42] C. Deen, M.T. Whittaker, W. Harrison, C.M.F. Rae, S.J. Williams, Relating fundamental creep mechanisms in Waspaloy to the Wilshire equations, MATEC Web Conf. (2014).

[43] H. Wang, Role of size and amount of γ` phase on creep properties of Waspaloy, Mater Charact (2021).

[44] M. Whittaker, W. Harrison, C. Deen, C. Rae, S. Williams, Creep deformation by dislocation movement in waspaloy, Materials 10 (2017) 61, https://doi.org/10.3390/ma10010061.

[45] K.-M. Chang, X. Liu, Effect of γ′ content on the mechanical behavior of the WASPALOY alloy system, Mater. Sci. Eng. A 308 (2001) 1–8, https://doi.org/10.1016/S0921-5093(00)02042-6.

[46] A. Chamanfar, M. Jahazi, J. Gholipour, P. Wanjara, S. Yue, Mechanical property and microstructure of linear friction welded WASPALOY, Metall. Mater. Trans. A 42 (2011) 729–744, https://doi.org/10.1007/s11661-010-0457-2.

[47] M. Göken, M. Kempf, Microstructural properties of superalloys investigated by nanoindentations in an atomic force microscope, Acta Mater. 47 (1999) 1043–1052, https://doi.org/10.1016/S1359-6454(98)00377-2.

[48] M.E. Kassner (Ed.), Fundamentals of Creep in Metals and Alloys, 2nd ed,., Elsevier, Amsterdam London, 2009.

[49] R.C. Reed, The Superalloys: Fundamentals and applications, Cambridge University Press, Cambridge, 2006, 10.1017/CBO9780511541285.

[50] L. Heep, D. Bürger, C. Bonnekoh, P. Wollgramm, A. Dlouhy, G. Eggeler, The effect of deviations from precise [001] tensile direction on creep of Ni-base single crystal superalloys, Scr. Mater. 207 (2022) 114274, https://doi.org/10.1016/j.scriptamat.2021.114274.

[51] J.H. Chen, P.M. Rogers, J.A. Little, Oxidation behavior of several chromia-forming commercial nickel-base superalloys, Oxid. Met. 47 (1997) 381–410, https://doi.org/10.1007/BF02134783.

[52] G.B. Viswanathan, D.E. Mills, M.J. Mills, Oxidation-related microstructural changes at a crack tip in waspaloy after elevated-temperature dwell-fatigue testing, Metall. Mater. Trans. A 50 (2019) 5574–5580, https://doi.org/10.1007/s11661-019-05499-0.

[53] S.A.J. Forsik, A.O. Polar Rosas, T. Wang, G.A. Colombo, N. Zhou, S.J. Kernion, M. E. Epler, High-temperature oxidation behavior of a novel Co-base superalloy, Metall. Mater. Trans. A 49 (2018) 4058–4069, https://doi.org/10.1007/s11661-018-4736-7.

[54] H.J. Frost, M.F. Ashby, Deformation-mechanism maps: the plasticity and creep of metals and ceramics, 1st ed,, Pergamon Press, Oxford [Oxfordshire]; New York, 1982.

[55] Y. Zhu, C. Li, Y. Liu, Z. Ma, H. Yu, Effect of Ti addition on high-temperature oxidation behavior of Co–Ni-based superalloy, J. Iron Steel Res. Int. 27 (2020) 1179–1189, https://doi.org/10.1007/s42243-020-00379-z.

[56] Z. Li, Y. Hong, Y. Li, W. Qin, X. Wu, Improvement of oxidation resistance of the Ti-modified Cr-based coating on Zry-4 by Cr2O3/Cr2TiO5 double oxide layer with coherent interface, Surf. Coat. Technol. 496 (2025) 131612, https://doi.org/10.1016/j.surfcoat.2024.131612.

[57] The Materials Project, Materials Data on Cr2O3 by Materials Project, (2020). https://doi.org/10.17188/1194409.

[58] The Materials Project, Materials Data on Ti2CrO5 by Materials Project, (2020). https://doi.org/10.17188/1194376.

[59] The Materials Project, Materials Data on TiO2 by Materials Project, (2020). https://doi.org/10.17188/1184648.

[60] J. Dai, J. Zhu, C. Chen, F. Weng, High temperature oxidation behavior and research status of modifications on improving high temperature oxidation resistance of titanium alloys and titanium aluminides: a review, J. Alloy. Compd. 685 (2016) 784–798, https://doi.org/10.1016/j.jallcom.2016.06.212.

[61] I.C.I. Okafor, R.G. Reddy, The oxidation behavior of high-temperature aluminides, JOM 51 (1999) 35–40, https://doi.org/10.1007/s11837-999-0092-9.

[62] M.P. Brady, W.J. Brindley, J.L. Smialek, I.E. Locci, The oxidation and protection of gamma titanium aluminides, JOM 48 (1996) 46–50, https://doi.org/10.1007/BF03223244.

[63] F. Guler, A.A. Inceyer, S. Kol, M. Usta, H. Aydin, O. Keles, Improving cyclic oxidation resistance of additively manufactured in939 superalloy via chemical vapor aluminizing, Adv. Eng. Mater. 27 (2025) 2402805, https://doi.org/10.1002/adem.202402805.

[64] S. Cruchley, H. Evans, M. Taylor, An overview of the oxidation of Ni-based superalloys for turbine disc applications: surface condition, applied load and mechanical performance, Mater. High Temp. 33 (2016) 465–475, https://doi.org/10.1080/09603409.2016.1171952.